

# Atomistic-Level Analysis of Nanoindentation-Induced Plasticity in Arc–Melted NiFeCrCo Alloys: The role of stacking faults

F. J. Domínguez-Gutiérrez,<sup>1</sup> A. Olejarz,<sup>1</sup> M. Landeiro Dos Reis,<sup>2</sup> E. Wyszowska,<sup>1</sup> D. Kalita,<sup>1</sup> W. Y. Huo,<sup>1</sup> I. Jozwik,<sup>1</sup> L. Kurpaska,<sup>1</sup> S. Papanikolaou,<sup>1</sup> M. J. Alava,<sup>1</sup> and K. Muszka<sup>3</sup>

<sup>1</sup>*NOMATEN Centre of Excellence, National Center for Nuclear Research, 05-400 Swierk/Otwock, Poland*

<sup>2</sup>*LaSIE UMR CNRS 7356, La Rochelle Université, Av. Michel Crépeau, 17042, La Rochelle Cedex 1, France*

<sup>3</sup>*AGH University of Science and Technology, al. Mickiewicza 30, 30-059 Kraków, Poland*

(Dated: 31 January 2024)

Concentrated solid solution alloys (CSAs) have attracted attention for their promising properties; however, current manufacturing methods face challenges in complexity, high costs, and limited scalability, raising concerns about industrial viability. The prevalent technique, arc melting, yields high-purity samples with complex shapes. In this study, we explore nanoindentation tests at room temperature where arc-melted samples exhibit larger grain sizes, diminishing the effects of grain boundaries on the results. Motivated by these findings, our investigation focuses on the atomistic-level exploration of plasticity mechanisms, specifically dislocation nucleation and propagation during nanoindentation tests. The intricate chemistry of NiFeCrCo CSA influences pile-ups and slip traces, aiming to elucidate plastic deformation by considering both pristine and pre-existing stacking fault tetrahedra. Our analysis scrutinizes dynamic deformation processes, defect nucleation, and evolution, complemented by stress-strain and dislocation densities-strain curves illustrating the hardening mechanism of defective materials. Additionally, we examine surface morphology and plastic deformation through atomic shear strain and displacement mappings. This integrated approach provides insights into the complex interplay between material structure and mechanical behavior, paving the way for an enhanced understanding and potential advancements in CSA applications.

Keywords: Dislocation plasticity mechanisms, Dislocations dynamics, SFT, Nanoindentation, high entropy alloy

## I. INTRODUCTION

High- and medium-entropy alloys (HEAs/MEAs) are a focal point of research due to the extensive variety of available elements, offering adaptable deformation behaviors<sup>1–6</sup>. While HEAs/MEAs have sparked substantial interest, systematic studies on their mechanical properties, particularly in well-controlled microstructures, have been nowadays an interesting topic for applications at extreme operating environments<sup>7–11</sup>. Despite challenging comparisons with conventional alloys, HEAs exhibit similar deformation mechanisms, offering a foundation to develop advanced alloys<sup>12–15</sup>. HEAs produced through arc melting technique after some plastic and heat treatments showcase highly promising characteristics across diverse applications, often exceeding initial expectations. The lattice distortion strengthening effect, typical for HEAs, further contributes to interstitial–vacancy recombination, reinforcing the alloy’s radiation resistance<sup>14</sup>. By bridging knowledge gaps, the community can unlock the potential of HEAs, achieving a harmonious synergy of multiple mechanisms for improved mechanical properties essential for structural applications<sup>6,7,16–18</sup>.

A category of materials referred to as single-phase concentrated solid-solution alloys (SP-CSAs), including High Entropy Alloys (HEAs)<sup>16,19,20</sup>, has recently attracted considerable attention due to their distinctive structures and exceptional properties. Unlike traditional alloys, SP-

CSAs are composed of two to five principal elements in nearly equal molar ratios, forming random solid solutions in either a simple face-centered cubic crystal lattice structure<sup>21</sup>. The intricate random arrangement of alloying elements and the local chemical environment at the atomic level contribute to the extraordinary properties exhibited by SP-CSAs compared to conventional alloys<sup>19,20</sup>. An exemplary four-element FeCrCoNi alloy<sup>22</sup> is recognized for its superior strength compared to FeNiCoMn. This alloy demonstrates impressive tensile strength and ductility achieved through sustained work hardening, and its fabrication holds significance for applications in extreme operating environments<sup>14</sup> being the material of interest in our work. The exceptional characteristics of SP-CSAs, as exemplified by this specific alloy, underscore their potential significance in advancing materials science for a range of demanding applications<sup>14,22</sup>.

Nanoindentation serves as a crucial technique for assessing the mechanical properties of potential candidate materials at the nanoscale, particularly for applications in extreme operating conditions. This method involves inserting a small, sharp tip into the sample surface to measure the force required and the resulting displacement within the material<sup>16,17,23–27</sup>. The occurrence of a pop-in event, marking the transition from elastic to plastic deformation as the indenter tip penetrates the surface, is often used as a reference point for analyzing a material’s mechanical behavior<sup>25</sup>. This event provides insights

into the internal structure of the sample, allowing for an exploration of the mechanisms responsible for plastic deformation initiation and subsequent modification of the material's mechanical properties<sup>28,29</sup>. Furthermore, nanoindentation-induced plastic patterning is a process that creates patterns or structures at the nanoscale, with applications ranging from fabricating nanostructured surfaces with enhanced functionalities to developing new materials with tailored mechanical properties<sup>30</sup>. The resulting plastic patterning is influenced by factors such as applied load, crystal orientation, temperature, and material properties, requiring a fundamental understanding of material deformation within the plastic zone beneath the indented surface region<sup>24,31</sup>. However, the mechanical response of materials is inherently tied to the extensive array of defects present within the material. Models can aid in decoupling the effects observed experimentally, although they present a challenge since modeling sufficiently large systems is complex to account for a diverse distribution of defects. Among these defects, stacking fault tetrahedra form more easily in High Entropy Alloys (HEA) compared to conventional alloys due to the lower stacking fault energy in these alloys<sup>32-34</sup>. Hence, in this paper, we choose to focus on this peculiar defect. We investigate both scenarios, with and without stacking fault tetrahedra, to examine the impact of this defect on the mechanical response of HEA.

In our comprehensive study, we conducted both experimental and computational investigations on NiFeCrCo high entropy alloys being prepared using the arc melting technique, followed by high-temperature homogenization process, which is the common methodology for high-entropy alloys' manufacturing. In the computational aspect of our study, we considered the composition derived from experimental data along with preexisting stacking faults tetrahedra. This allowed us to model the nanomechanical response of defected samples during nanoindentation tests. Our computational analysis involved reporting dislocation densities, mechanical responses through stress-strain curves, and examining the surface morphology of indented samples<sup>31</sup>. This integrated approach provides a comprehensive understanding of the material's behavior under nanoindentation conditions.

## II. EXPERIMENTAL METHODS

In our experimental investigation, a composition of Co, Cr, Fe, and Ni pieces were mixed in Ar-glovebox, followed by melting using an Edmund Buehler AM200 arc melting device equipped with Copper-mould. The furnace was evacuated up to  $5 \times 10^{-5}$  mbar and backfilled with Argon gas to a pressure of 600 mbar. To ensure the homogeneity, sample was flipped and remelted at least six times. Sample was homogenized in muffle furnace at 1200°C for 4 hours to remove dendritic structure and to promote uniform distribution of all elements present. We characterize the obtained NiFeCrCo sample via XRF technique

obtaining a chemical composition (in wt.%) of 26 % Ni, 25 % Fe, 26 % Co, and 22 % Cr. The amount of all impurities did not exceed 1 %. To characterize mechanical properties, nanoindentation using a NanoTest Vantage system with a Synton-MDP diamond Berkovich-shaped indenter was performed. Tests used a 150 mN load, with 100 indentations on sample at 100  $\mu\text{m}$  spacing.

### A. Structural characterization

The microstructural evolution of homogenized sample was investigated using the ThermoFisher Helios 5 UX scanning electron microscope. This advanced microscope is equipped with the EDAX Velocity Pro EBSD camera, enabling precise crystal orientation mapping. EBSD mapping was performed with a 0.25  $\mu\text{m}$  step size. The acquired data underwent thorough analysis using the EDAX OIM Analysis 8 software, with points having a confidence index (CI) below 0.1 being excluded from calculations.

## III. COMPUTATIONAL METHODS

To perform our simulations, we use the Large-scale Atomic/Molecular Massively Parallel Simulator (LAMMPS) software<sup>35</sup>, which allows us to study the behavior of materials under a wide range of conditions. One of our goals is to accurately model plastic deformation, which is a crucial aspect of how materials respond to external loads. Thus, we utilize interatomic potentials reported by Choi et al.<sup>36</sup>; which are based on the second Nearest Neighbor Modified Embedded Atom Method (2NN-MEAM) as reported in our previous work<sup>16,17,37</sup>.

We initially defined the FCC Ni sample with crystal orientations along [001], [101], and [111], followed by the optimization of the system's energy using The FIRE (Fast Inertial Relaxation Engine) 2.0 protocol<sup>38</sup> to identify the lowest energy structure<sup>16,31,39,40</sup>. The equilibration continued until the system achieved homogeneous temperature and pressure profiles at a density of 8.23  $\text{g}/\text{cm}^3$ , in good agreement with the experimental value<sup>29</sup>. A final step involved relaxing the prepared sample for 10 ps to dissipate any artificial heat. To create the FCC CSA, randomness was introduced by substituting 75% of Ni atoms from the original sample, oriented in different crystal directions, for 26 % Ni, 25 % Fe, 26 % Co, and 22 % Cr in wt, following the experimental results. The optimization process for the samples' geometry is directed towards the nearest local minimum of the energy structure. The optimization criteria include ensuring that the change in energy between successive iterations and the most recent energy magnitude remains below  $10^{-5}$ . Additionally, the global force vector length of all atoms is maintained at less than or equal to  $10^{-8}$  eV/Å. The subsequent steps for preparing the sample mirrored those of the pristine case, resulting in an equiatomic NiFeCrCoMn CSA.

In agreement with the Silcox and Hirsch mechanism, stacking fault tetrahedra (SFT) can be formed from an equilateral triangular vacancy plate situated on the (111) planes<sup>41</sup>. To construct HEA-CSA with pre-existing SFT, we initiate the process by introducing four vacancy plates within the (111) planes beneath the surface (See Fig. 1.)<sup>42</sup>. The subsequent energy minimization prompts the plates to undergo transformation into SFTs, characterized by stair-rod dislocations (depicted by the yellow line on the SFTs Fig. 1.) and a hexagonal close-packed (HCP) structure between these dislocations (atoms colored in blue Fig. 1.). Various scenarios were examined to investigate the impact of SFT size and distribution. The configurations considered include one without any SFT, followed by configurations with four SFTs of 1 nm size, four SFTs of 4 nm size, and, lastly, four SFTs with sizes of 1 nm, 2 nm, 3 nm, and 4 nm, respectively.

During the initial stage, the CSA samples underwent division into three distinct sections along the  $z$  direction to establish boundary conditions along their depth, denoted as  $d_z$ : 1. Frozen Section: A stabilizing frozen section, approximately  $0.02 \times d_z$  in width, was implemented to ensure the numerical cell's stability. 2. Thermostatic Section: Positioned roughly  $0.08 \times d_z$  above the frozen section, this thermostatic section was dedicated to dissipating heat generated during the nanoindentation process. 3. Dynamical Atoms Section: This section allowed for dynamic interaction with the indenter tip, resulting in modifications to the surface structure of the samples. Additionally, a 5 nm vacuum section was incorporated at the top of the sample, serving as an open boundary<sup>16,39,43</sup>.

Within the spatial (few nanometers) and temporal (picoseconds) scales of the MD simulations, nanoindentation testing allows for the examination of the initial stages of plastic deformation and phase transformation at the atomic level. In the numerical modeling, a Berkovich tip can be effectively represented by a spherical indenter tip due to the minimal distinctions observed in the phase transformation regions of both tips during the early stages of the loading process<sup>16,24</sup>. The indenter tip is defined as a non-atomic repulsive imaginary (RI) rigid sphere, exerting a force of magnitude  $F(t) = K(r(t) - R_i)^2$  on each atom. In this equation,  $K = 200 \text{ eV}/\text{\AA}^3$  denotes the specified force constant, ensuring high stiffness for our indenter tip<sup>39</sup>. The parameter  $r(t)$  represents the

TABLE I. Size of the initial numerical samples used to perform MD simulations of pristine HESSA<sup>17</sup>. Sample size ( $d_x$ ,  $d_y$ ,  $d_z$ ) in units of nm.

Orientation	[001]	[011]	[111]
$d_x$	33.20	33.06	33.07
$d_y$	36.09	36.17	36.12
$d_z$	36.12	38.17	40.61
Atoms	3 164 800	3 442 032	3 645 720
X-axis	(100)	(100)	( $\bar{1}01$ )
Y-axis	(010)	(01 $\bar{1}$ )	( $1\bar{2}1$ )
Z-axis	(001)	(011)	(111)

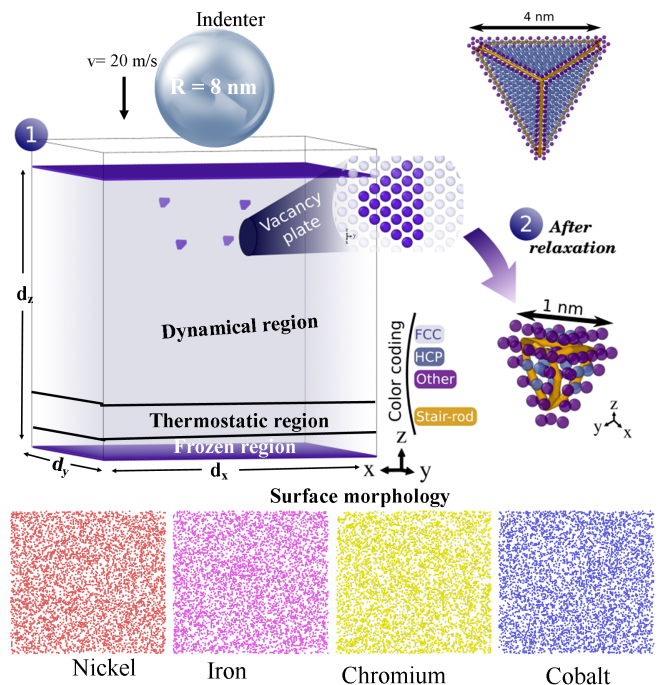


FIG. 1. (Color online) Simulation cell exhibiting four vacancy plates, each measuring 1 nm in size. Upon relaxation, these plates undergo transformation into a stacking fault tetrahedra (SFT). Additionally, a 4 nm-sized SFT is included for comparison. Initial frame of the nanoindentation simulation, emphasizing the stacking fault tetrahedron and stair-rod dislocations near the surface. To enhance visual clarity, an atom with an FCC lattice position has been removed. The surface top view showcases the atomic arrangement of the five types of atoms: Ni, Fe, Cr, Co, and Mn and the indents. Additionally, the sample is strategically divided into three sections—frozen, thermostatic, and dynamical to facilitate the mechanical test.

distance from the atoms to the center of the indenter, and  $R_i = 8 \text{ nm}$  is the radius of the indenter, chosen to be sufficiently large to accurately model the elastic-to-plastic deformation transition<sup>43</sup>. The initial location of the tip is set at a separation distance of 0.5 nm from the material's surface, and its center is randomly shifted to ten different positions to account for statistical variation, as depicted by black dots in Fig. 1. We employ an NVE statistical thermodynamic ensemble with the velocity Verlet algorithm for an indenter speed of  $v = 20 \text{ m/s}$  for 125 ps, using a time step of  $\Delta t = 1 \text{ fs}$ . A maximum indentation depth of  $h_{\text{max}} = 2.0 \text{ nm}$  is selected to minimize boundary layer effects in the dynamic atoms region<sup>16</sup>. The initial configuration of the nanoindentation simulation is illustrated in Fig. 1.

#### IV. RESULTS

We conducted experimental nanoindentation tests on a polycrystalline NiFeCrCo alloy, with a detailed exam-

ination involving the mapping of 100 nanoindentations. The investigation extends beyond the mechanical tests to explore crystallographic effects on the plastic deformation of the material. Utilizing EBSD imaging, we obtained insights into the propagation of pile-ups within various slip planes. The EBSD images of the [001] and [101] orientations are presented in Fig 2(a-b). The emission of surface slip traces is a crucial manifestation of crystal plasticity, providing essential insights for a comprehensive understanding of the mechanical response of materials. EBSD analysis of the samples reveals slip traces for  $\{110\}$  indenter planes in  $\langle 112 \rangle$  directions (Fig. 2(b)). A close-up of the [101] orientation of the alloy provides additional detail, showcasing the propagation of slip traces on  $\{211\}$  planes—features typically observed in FCC (Face-Centered Cubic) materials and in a good agreement with our MD simulations. This arises from the interaction between dislocation gliding in  $\{111\}$  planes and the indenter surfaces in the  $\{110\}$  plane<sup>24</sup>. Similarly, when considering  $\{100\}$  indenter planes, only slip traces aligned in  $\langle 110 \rangle$  directions can be produced through its interaction with dislocation gliding in  $\{111\}$  planes (Fig. 2(a)). The grain with [101] orientation presents a little higher hardness, the difference does not exceed 4% (1.69 GPa vs 1.63 GPa). The crystallographic aspects of the deformation process

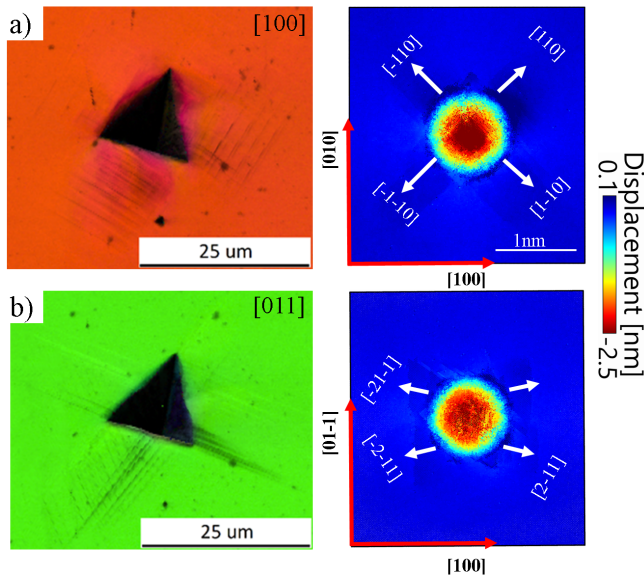


FIG. 2. (Color online) EBSD image of (a) [001] and (b) [011] orientation identified by the IPF mapping. The images revealing crystallographic effects on the plastic deformation of the polycrystalline NiFeCrCo alloy. The image showcases the propagation of pile-ups across different slip planes, providing insights obtained from mapping 100 nanoindentations in the experimental nanoindentation tests. Observation of slip-traces and pile-ups formation at a maximum indentation depth of 3 nm for the [100] and [011] orientations obtained by MD simulations are presented next to experimental images. The propagation of slip traces is indicated by their corresponding planes, exhibiting typical rosette shapes characteristic of FCC metals.

provide a comprehensive understanding of the material's response to nanoindentation. This combined approach of nanoindentation and EBSD imaging contributes valuable data to elucidate the intricate mechanics of plastic deformation in the NiFeCrCo alloy.

As discussed, the experimental nanoindentation test motivates the computational modeling to explore the plastic deformation mechanism in the NiFeCrCo CSA at different crystal orientations. The morphology of the indented samples is assessed by calculating atomic displacements concerning the initial frame in our MD simulations. In Fig. 2(a-b), slip traces and pile-up formations for the NiFeCrCo CSA are depicted at [001] and [011] orientations, reaching a maximum indentation depth of 3 nm. The observed propagation of slip traces aligns with the slip planes of the face-centered cubic (FCC) sample at each crystal orientation. Notably, the 4-fold shapes for [001] and [011] correspond to typical shapes exhibited by FCC metals<sup>16,24</sup>. Building on our prior research<sup>17</sup>, we highlight the distinctive effect of the four elements in the CSA alloy, forming a halo around the indenter tip irrespective of crystal orientation. In contrast, single-element FCC metals typically result in step-shaped pile-ups. This behavior is attributed to the intricate chemistry of the CSA alloy.

The implementation of the numerical modeling for nanoindentation tests is done in accordance to experimental conditions by tracking atomic strains and dislocation network dynamics. Fig. 3 reports the mean contact pressure  $p$ , of the pristine CSA as a function of the nanoindentation depth which is obtained by<sup>28,43,44</sup>:

$$p(h) = \frac{2\pi}{3E_Y} \left[ 24P_{\text{ave}}(h) \left( \frac{E_Y R_i}{1 - \nu^2} \right)^2 \right]^{1/3}, \quad (1)$$

where  $h$  is the indentation depth,  $\nu$  is the Poisson's ratio, and the average load is calculated as  $P_{\text{ave}}(h) = 1/N \sum_i^N P_i(h)$  with  $P_i(h)$  as the load from each MD simulation and  $N = 10$  the number of indents. During loading process, the contact radius is obtained with the geometrical relationship as<sup>43</sup>:

$$a(h) = \left[ 3P_{\text{ave}}(h) R_i \frac{1 - \nu^2}{8E_Y} \right]^{1/3}, \quad (2)$$

these quantities provide an intrinsic measure of the surface resistance to defect nucleation<sup>24,43</sup> and yield to a universal linear relationship between  $p(h)/E_Y$  and  $a(h)/R_i$  given by

$$\frac{p(h)}{E_Y} = \frac{0.844}{1 - \nu^2} \frac{a(h)}{R_i}. \quad (3)$$

which is shown in the Fig 3 by a green line. Hence, the pop-in event can be characterized as the departure of the contact pressure curve from the linear scaling law that describes the transition from the elastic to the plastic deformation region. It is noteworthy that the occurrence

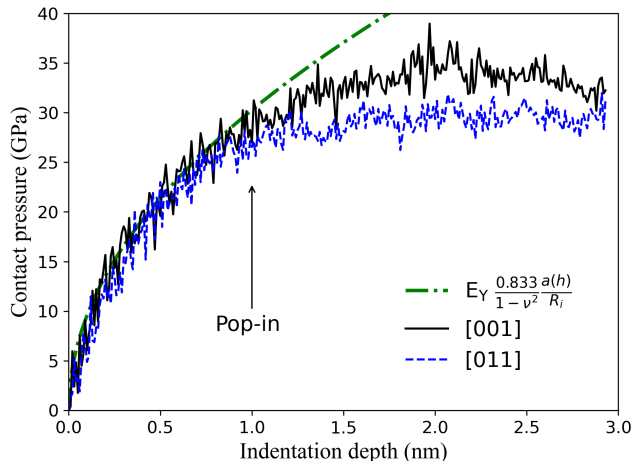


FIG. 3. (Color online) Average contact pressure as a function of indentation depth for the pristine NiFeCrCo sample at [001], [101], and [111] orientations in (a), with the pop-in event identified as a deviation from the linear scaling law.

of this event is contingent upon the crystallographic orientation of the material where the critical load is higher for [001] than the one for [011] orientation.

In order to analyze the influence of the crystal orientation on the dislocation nucleation and evolution of the sample, we visualize and quantify different types of dislocations nucleated at different indentation depths by using the OVITO<sup>45</sup> software. This was done through the use of the Dislocation Extraction Algorithm (DXA)<sup>46</sup>; that extracts dislocation structure and content from atomistic microstructures. Thus, we categorized the dislocations into several dislocation types according to their Burgers vectors as:  $\frac{1}{2}\langle 110 \rangle$  (Perfect),  $\frac{1}{6}\langle 112 \rangle$  (Shockley),  $\frac{1}{6}\langle 110 \rangle$  (Stair-rod),  $\frac{1}{3}\langle 100 \rangle$  (Hirth),  $\frac{1}{3}\langle 111 \rangle$  (Frank) noticing that the nucleation of partial  $\frac{1}{6}\langle 112 \rangle$  Shockley dislocations is dominant in the loading process regardless of the crystal orientation due to the material's FCC structure. Thus, we compute the dislocation density,  $\rho$ , as a function of the depth as:

$$\rho = \frac{N_D l_D}{V_D}, \quad (4)$$

where  $N_D$  is the number of dislocation lines and loops measured during nanoindentation test;  $l_D$  is the dislocation length of each type, and  $V_D = 2\pi/3(R_{pl}^3 - h^3)$  is the volume of the plastic deformation region by using the approximation of a spherical plastic zone; where  $R_{pl}$  is the largest distance of a dislocation measured from the indentation displacement, considering a hemispherical geometry.

In Fig. 4 we present the average of the dislocation density as a function of the indentation depth for the [001] in a) and [011] in b) crystal orientation. It is observed that the Shockley dislocation is nucleated and evolved during the whole loading process, as expected. The interaction of

different Shockley dislocations can lead to the nucleation of Hirth and Stair-rod dislocation as follows:

$$\frac{1}{3}[100] = \frac{1}{6}[12\bar{1}] + \frac{1}{6}[1\bar{2}1] \quad \text{Hirth}, \quad (5)$$

$$\frac{1}{6}[110] = \frac{1}{6}[\bar{1}21] + \frac{1}{6}[2\bar{1}\bar{1}] \quad \text{Stair-rod}, \quad (6)$$

and other symmetrical cases. As the primary dislocation junctions manifest during the loading process, this mechanism is recognized for its role in initiating the nucleation of prismatic dislocation loops. This initiation is discerned as a decrease in the total dislocation density at 1.1 nm across all orientations. Additionally, the nucleation of dislocations commences at a depth of 0.75 nm for [001] and [011] orientations. This discrepancy is attributed to the distinct atomic arrangement within the unit cell of each orientation. Moreover, it is noteworthy that the density of Shockley partials tends to rise for the  $\{100\}$  indenter plane, in contrast to the slight decrease observed in the case of the  $\{110\}$  indenter plane. This phenomenon may be partially explained by the strong interaction of these dislocations with the  $\{110\}$  plane, leading to their annihilation, as evidenced by the slip traces shown Fig.

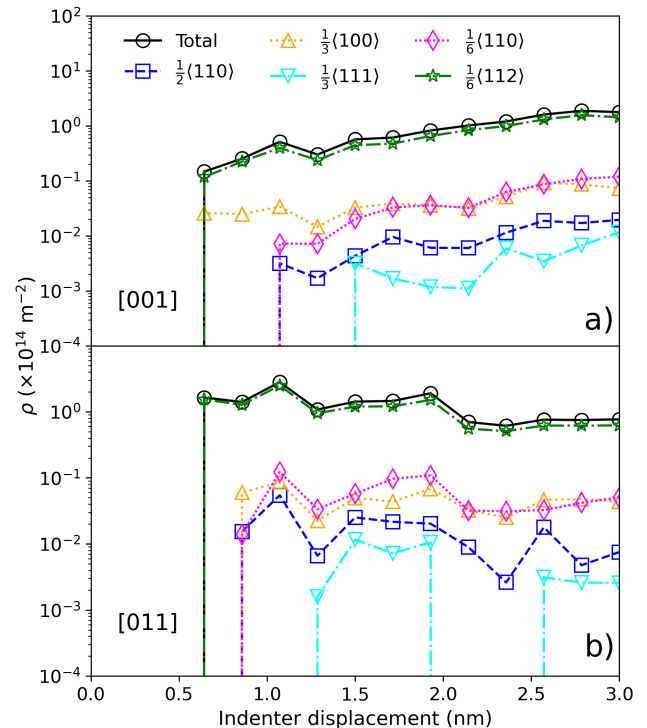


FIG. 4. (Color online) Average dislocation density plotted against the indentation displacement for [100] and [011] crystal orientations in (a) and (b), respectively. Notable crystallographic effects are evident in dislocation nucleation. As anticipated, Shockley dislocations predominantly nucleate and evolve throughout the entire loading process, with their interactions giving rise to stair-rod and Hirth junction dislocation nucleation.

2(b).

At the maximum indentation depth, we observe parallels between the NiFeCrCo CSA and those exhibited by single-element face-centered cubic (FCC) metals, such as Ni<sup>16,24</sup>, as depicted in Fig. 5. Figure 5a) illustrates the formation of a nano-twin beneath a [101] surface, with black lines denoting parent and twinned crystal orientations. This observation aligns well with the typical mechanisms observed in FCC metals. Importantly, our findings reveal that atomic ordering is not a prerequisite for this mechanism. Furthermore, twin nucleation in our sample is initiated under the strain gradients and stresses imposed by the nanoindenter tip. This involves the successive emission of leading partial dislocations in the vicinity of the indenter, resulting in the distinctive arrangement of parallel {111} twinned planes<sup>47,48</sup>. Our simulations demonstrate that the twin boundaries are normal to the surface for (011) indentation and inclined at 135.25°. The twinning crystallography ensures that all  $\langle 011 \rangle$  and  $\langle 112 \rangle$  traces simultaneously lie at the indented plane and a specific {111} habit plane, conforming to expectations for FCC metals.

In Fig. 5b, we illustrate the prismatic dislocation loop at the maximum indentation depth for the [101] crystal orientation. Notably, the observation reveals that the junction of Shockley partial dislocations leads to the final state of the formation of this loop, accompanied by stacking fault planes identified as hexagonal close-packed (HCP) atoms. This identification is made through Polyhedral Template analysis in Ovito. The atoms involved are color-coded based on their types, enabling an analysis of their random distribution maintained during the loading process. Importantly, no specific ordering of atoms was observed throughout this process.

Nevertheless, in comparison to pure Ni, all defects are

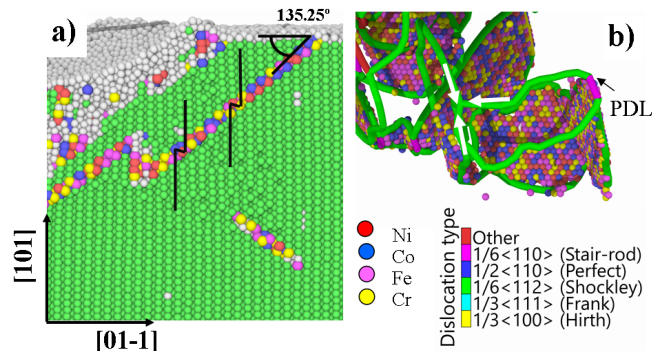


FIG. 5. (Color online) Cross-sectional view of a nanotwin underneath a [101] surface in (a); black lines indicate parent and twinned crystal orientations for enhanced visualization, illustrating the well-known nanotwin mechanism in FCC metals. Formation of a prismatic dislocation loop in the [101] orientation at an indentation depth of 2 nm; white arrows indicate the dislocation junction. FCC atoms are removed, and only atoms with HCP structure corresponding to stacking fault planes are displayed for clarity.

confined to a narrow region beneath the surface, possibly attributed to the reduced dislocation velocity in HEA<sup>49</sup>. That can be correlate to the typical hallow observed around the indenter tip a contrario to the larger step-shaped piles ups observed in pure Ni<sup>16,17,50,51</sup>. In these alloys, dislocations exhibit a wavy morphology and encounter natural pinning points stemming from the variable chemical and energetic landscape surrounding the dislocation core. For the same reason twin boundary planes are expected to be more fragmented than in pure Ni<sup>50</sup>.

### A. Nanoindentation Modeling of defected NiFeCrCo CSA

The impact of the nanomechanical response in defected NiFeCrCo CSA is examined through the analysis of nanoindentation contact pressure as a function of indentation strain, comparing it to the pristine case for both [001] and [101] orientations, as depicted in Fig. 6. The

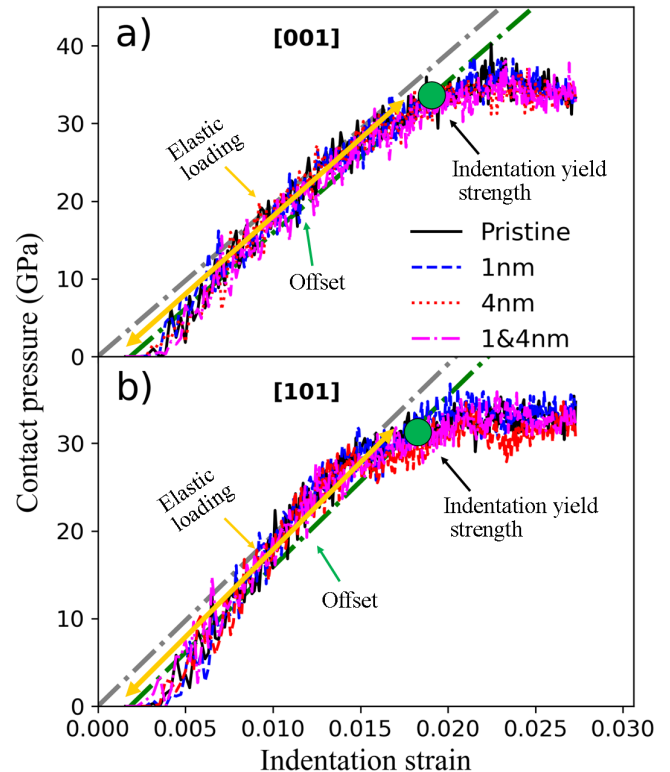


FIG. 6. (Color online) Average nanoindentation contact pressure as a function of indentation strain, comparing it with the pristine case for [001] and [101] orientations. The pressure-strain curve is characterized by contrasting it with a linear scaling law (gray dashed line), where the offset in nanoindentation strain due to the indenter tip speed is indicated by a green line. The pop-in event, marking the indentation yield strength, is identified as a deviation from the scaling law, denoted by a green spot. The plastic region exhibits a stable pressure at higher nanoindentation strain values.

pressure–strain curve is characterized by contrasting it with a linear scaling law to delineate the elastic loading phase. Due to the speed of the indenter tip, there is an offset in the nanoindentation strain, indicated by a green line. The occurrence of a pop–in event is identified as a deviation of the pressure curve from the scaling law, marked by a green spot, representing the indentation yield strength. Subsequently, the plastic region exhibits a stable pressure at higher nanoindentation strain values. Through the analysis of this material response during the loading process, it is observed that materials with preexisting Stacking Fault Tetrahedra (SFTs) experience an increase in hardness values and their maximum shear stress<sup>43</sup>. SFT impede the glide of dislocations, requiring them to find alternative paths to navigate around and pass through the SFT.

At the maximum indentation depth, the plastic deformation of the NiFeCrCo CSA sample induced by the indenter tip’s shear strain becomes evident. In Fig. 7, atomic shear strain mappings are presented for the [011] NiFeCrCo CSA sample under different conditions: pristine case in (a), 1 nm of SFTs in (b), 4 nm of SFT in (c), and a combination of SFTs in (d). The sample is visually enhanced by slicing it in half, and the width of the “lamella” is halved for better visualization. For the pristine case, maximum strain accumulates underneath the indenter tip, and slip planes are delineated by an increase in strain value relative to the FCC atoms (colored in blue). In contrast, when SFTs are present, strain accumulates on the surface for smaller SFTs, around the positions of 4 nm-sized SFTs, and beneath the indenter tip. This pattern persists for a mixed-size distribution of SFTs. Additionally, the triangular shape of the strained atoms varies with the size of the SFTs. While the pristine case exhibits a symmetric triangle, the presence of SFTs leads to asymmetric and sharper triangles due to

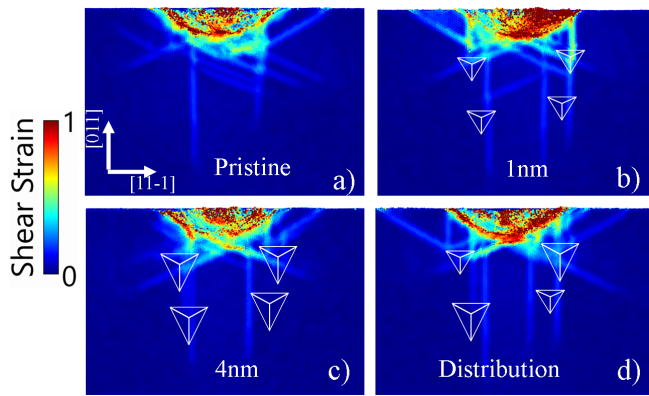


FIG. 7. (Color online) Atomic shear strain mapping of selected MD simulations of [101] NiFeCrCo alloy at the maximum indentation depth for pristine samples in (a), with 1nm stacking fault tetrahedra (SFTs) in (b), 4nm in (c), and SFTs at different sizes in (d). The influence of defect materials is evident in the accumulation of strain underneath the tip, affecting the propagation of dislocations.

the pre-existing strain fields around the defects. This effect, depending on the SFT size is challenging to understand and may be link to the complex interactions between the SFT, composed of stair rods dislocations and dislocations<sup>52</sup>. This phenomenon influences the nucleation and evolution of dislocations, shear, and prismatic dislocation loops.

In Fig. 8, a top-view of the samples at the maximum indentation depth is presented, where the preexisting SFT vacancy defects are indicated by dashed yellow lines. It is observed that, for the pristine cases, the nanotwin and stacking fault planes propagate on the [011] slip planes and symmetric families. However, in the defected samples, these planes interact with the preexisting vacancy defects, forming a cross-slip in combination with a [001] plane, which is developed in the region between the vacancy defects. This cross slip mechanisms, may arise from the interaction between the SFT and the screw dislocation segments. Previous atomistic simulations show that the dislocation screw constricts when it reaches the SFT and then cross slipped<sup>52</sup>. The interaction with edge dislocation segments leads to the formation of super-jogs, unstable that can lead to small vacancy clusters<sup>52</sup>.

To monitor the plastic deformation of the NiFeCrMn CSA during the loading process, we examine the sample at the [011] orientation, considering a size distribution for preexisting SFTs and calculating the dislocation density as a function of indentation displacement, as illustrated

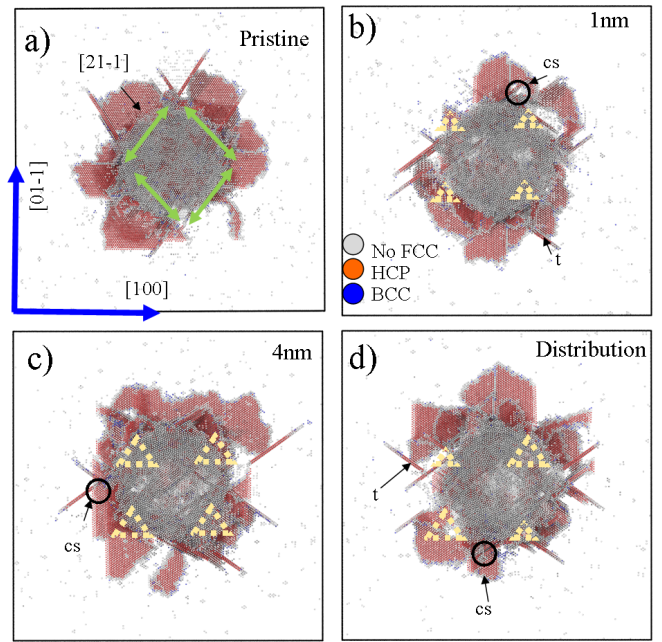


FIG. 8. (Color online) Top view of the atomic structure of [101] NiFeCrCo alloy for different samples (pristine, 1nm SFT, 4nm SFT, and a combination of 1 and 4 nm SFT; indicated by dashed orange lines). Slip planes are identified in the pristine case, while SFT promotes the formation of cross-slip, highlighted by black circles. Nanotwins are labeled with the letter “t.”

in Fig. 9. Our observations reveal that SFTs are predominantly formed by Stair-rod type dislocations, and Shockley-like half-loops initiate nucleation during the early stages of nanoindentation loading, occurring within the 0 to 1.0 nm depth range, as depicted in the inset of the figure. As the indentation progresses to greater depths, from 1nm to 2nm, Shockley dislocations interact with the stair rods of the SFT, absorbing them, while the stacking plane propagates due to the stress applied by the indenter tip. Upon reaching the maximum indentation depth, the larger-sized SFTs are already absorbed by the stacking fault planes induced by nanoindentation. Only smaller-sized SFTs survive the entire process, either by being pushed downward or by not interacting with the stacking fault planes.

## B. The case of nanoindentation on the [111] orientation

Although the experimental nanoindentation of the CSA on the [111] orientation is not often obtained, we analyze the mechanical response of the material on this specific orientation. The Stacking Fault Tetrahedra (SFTs) are generated on the habit {111} plane, aligning with the crystal orientation [111] in the NiFeCrCo CSA. This creates an excess of pressure during the loading process, attributed to the insertion of SFT vacancy types highlighted by yellow lines. Consequently, we conduct an analysis of the atomic structure evolution and dislocation behavior in both pristine and defected samples at various indentation

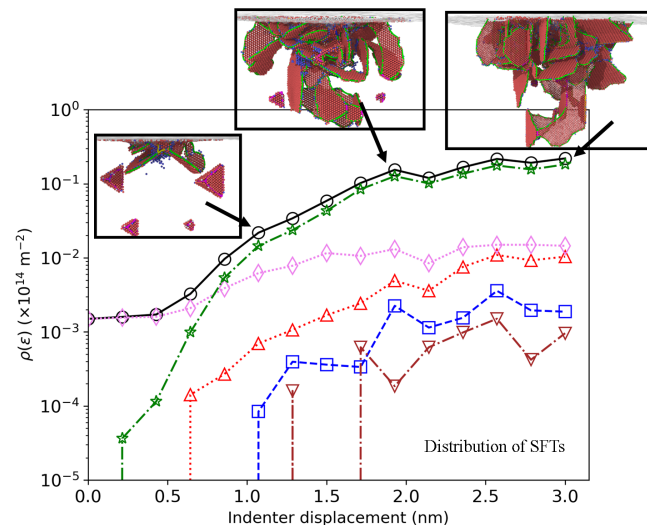


FIG. 9. (Color online) Dislocation density plotted against indentation displacement for the NiFeCrMn CSA on the [011] orientation, featuring a size distribution for preexisting stacking fault tetrahedra (SFTs). The figure includes visualizations of dislocation nucleation and evolution at every nanometer of displacement, along with the formation of stacking planes. Color code for dislocation type and atomic structure follows the one use for Fig. 4 and 8, respectively.

depths. In Fig. 10, we illustrate the evolution of stacking fault planes identified by hexagonal close-packed (HCP) atoms in orange, as well as the propagation of dislocations for the pristine case in (a) and SFT vacancy types in (b-d). At 1 nm depth, the pristine case nucleates a small stacking fault (SF) plane parallel to the {111} plane underneath the indenter tip, while the strain field induced by SFT vacancy types deforms this plane into a pair of half loops beneath the indenter tip. At 2 nm depth, the pristine case shows a nanotwin emerging from the side of the indenter tip, while a twin boundary (TB) forms in samples with SFT vacancy types. For smaller SFTs, the half loops do not yet interact with the defects, but for a distribution of SFT vacancy sizes, interactions with larger SFTs are observed.

At the maximum indentation depth of 3 nm, the pristine case has already initiated the nucleation of a complete prismatic dislocation loop (PDL) and a small twin boundary (TB). In contrast, the 1 nm Stacking Fault Tetrahedra (SFT) case exhibits the formation of a larger TB above the location of the SFT vacancies, and a small PDL is also nucleated in the direction where the SFT vacancies are absent. For larger 4 nm SFTs and a combination of SFT vacancies, the TB plane becomes larger, and PDLs begin to form in the same direction where there are no preexisting defects. These mechanisms have a significant

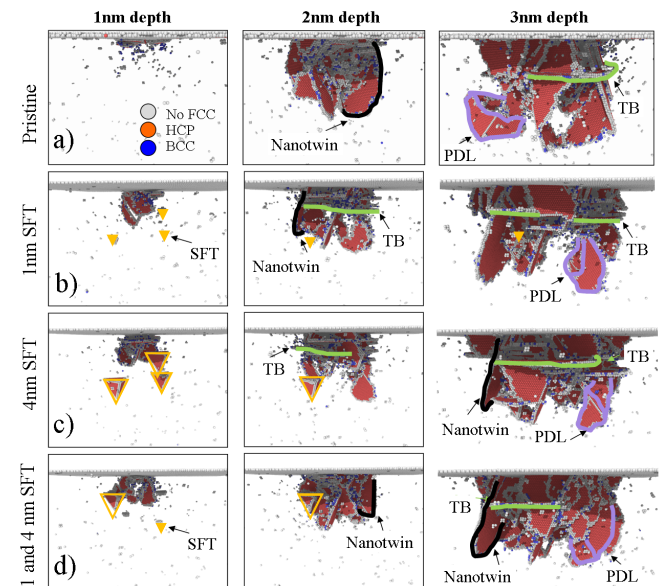


FIG. 10. (Color online) Atomic structure visualization of [111] NiFeCrCo pristine and with preexisting stacking fault tetrahedra (SFTs) at different indentation depths: 1nm in (a), 2nm in (b), and 3nm in (c). FCC atoms are removed to illustrate the evolution of stacking fault planes as hexagonal close-packed (HCP) atoms, with nanotwins highlighted by black lines, twin boundaries depicted as green lines, and prismatic dislocation loops (PDLs) represented by violet lines. The influence of defected alloys is evident as strain at the surface alters the direction of plane propagation and induces PDL formation.



impact on the nanomechanical response of the material, resulting in a load-displacement curve that is noisy and challenging to analyze for the defected cases. The presence of SFTs at different depths induces interactions that influence dislocation nucleation and evolution. Consequently, the resulting load-displacement curve in defected cases presents a challenge for analysis due to its noisy response due to excess of strain in the surface in close connection to SFTs preexisting in the sample.

## V. CONCLUDING REMARKS

This study delves into the nanomechanical response of the crystalline NiFeCrCo concentrated solid solution alloy (CSA) through a comprehensive exploration employing both experimental and computational approaches in nanoindentation tests. In the experimental realm, the production and characterization of CSA leverage an arc melting technique. Subsequently, nanoindentation tests are conducted at room temperature, allowing for the acquisition of surface morphology through electron microscopy images. In parallel, atomistic computational modeling captures the nanoindentation loading process, recording load-displacement curves, dislocation densities, and mapping atoms displacements. Notably, dislocation nucleation mechanisms are present with the prismatic loop formation profoundly influenced by surface characteristics, stacking faults, and dislocation glide energies during the nanoindentation loading process. The experimental characterization of the NiFeCrCo CSA is in good agreement with MD simulations by showing similarities to the propagation of slip-traces and consecutive nucleation of prismatic dislocation loops.

In addition, the introduction of Stacking Fault Tetrahedra (SFT) vacancy type defects emerges as a transformative factor in shaping the nanomechanical behavior of the material. Crystallographic orientations stand out as pivotal elements influencing the evolution of dislocations and stacking fault planes during the loading process. Distinct behaviors observed in defected samples, including altered dislocation propagation and stacking fault planes, underscore the profound impact of crystallographic factors on the material's mechanical response.

Furthermore, the existence of preexisting SFT vacancy defects triggers interactions with dislocation planes, giving rise to phenomena such as cross-slip and the formation of additional slip planes, notably [101]. The emergence of twin boundaries, prismatic dislocation loops, and modifications to crystallographic families collectively illuminate the intricate interplay between crystallographic factors and defect structures. This interplay significantly influences the material's mechanical response during nanoindentation.

## ACKNOWLEDGEMENTS

Research was funded through the European Union Horizon 2020 research and innovation program under Grant Agreement No. 857470 and from the European Regional Development Fund under the program of the Foundation for Polish Science International Research Agenda PLUS, grant No. MAB PLUS/2018/8, and the initiative of the Ministry of Science and Higher Education 'Support for the activities of Centers of Excellence established in Poland under the Horizon 2020 program' under agreement No. MEiN/2023/DIR/3795. We gratefully acknowledge enlightening discussions with Xavier Feaugas. We would like to express our gratitude to NOETHER computing facilities at La Rochelle University and MCIA (Mésocentre de Calcul Intensif Atlantique). Additionally, we extend our gratitude to GENCI - (CINES/CCRT), under Grant number A0110913037.

## REFERENCES

- <sup>1</sup>C. Wagner, A. Ferrari, J. Schreuer, J.-P. Couzini, Y. Ikeda, F. Kärmmann, G. Eggeler, E. P. George, and G. Laplanche, *Acta Materialia* **227**, 117693 (2022).
- <sup>2</sup>Z. Li and et al., *Sci. Rep.* **7**, 40704 (2017).
- <sup>3</sup>W. Huo, F. Fang, H. Zhou, Z. Xie, J. Shang, and J. Jiang, *Scripta Materialia* **141**, 125 (2017).
- <sup>4</sup>H. Shahmir, J. He, Z. Lu, M. Kawasaki, and T. G. Langdon, *Materials Science and Engineering: A* **685**, 342 (2017).
- <sup>5</sup>K. Cichocki, P. Bala, T. Koziel, and et al., *Metall Mater Trans A* **53**, 1749–1760 (2022).
- <sup>6</sup>K. Frydrych, K. Karimi, M. Pecelerowicz, R. Alvarez, F. J. Dominguez-Gutiérrez, F. Rovaris, and S. Papanikolaou, *Materials* **14** (2021).
- <sup>7</sup>E. George, W. Curtin, and C. Tasan, *Acta Materialia* **188**, 435 (2020).
- <sup>8</sup>Q. F. He *et al.*, *Materials Research Letters* **5**, 300 (2017).
- <sup>9</sup>B. L. Music, D. Gilbert, T. Z. Ward, K. Page, E. George, J. Yan, D. Mandrus, and V. Keppens, *APL Materials* **8**, 040912 (2020).
- <sup>10</sup>J.-W. Yeh, S.-K. Chen, S.-J. Lin, J.-Y. Gan, T.-S. Chin, T.-T. Shun, C.-H. Tsau, and S.-Y. Chang, *Advanced Engineering Materials* **6**, 299.
- <sup>11</sup>R. Babilas, K. Mlynarek-Lak, A. Radol, W. Iolski, *et al.*, *Journal of Alloys and Compounds* **960**, 170839 (2023).
- <sup>12</sup>D. Miracle and O. Senkov, *Acta Materialia* **122**, 448 (2017).
- <sup>13</sup>W. Huo, F. Fang, X. Liu, S. Tan, Z. Xie, and J. Jiang, *Applied Physics Letters* **114**, 101904 (2019).
- <sup>14</sup>A. Olejarz, W. Huo, M. Zielinski, R. Diduszko, E. Wyszowska, A. Kosinska, D. Kalita, I. Janwik, M. Chmielewski, F. Fang, and L. Kurpaska, *Journal of Alloys and Compounds* **938**, 168196 (2023).
- <sup>15</sup>K. Karimi, H. Salmenjoki, K. Mulewska, L. Kurpaska, A. Kosinska, M. J. Alava, and S. Papanikolaou, *Scripta Materialia* **234**, 115559 (2023).
- <sup>16</sup>L. Kurpaska, F. Dominguez-Gutierrez, Y. Zhang, K. Mulewska, H. Bei, W. Weber, A. Kosinska, W. Chrominski, I. Jozwik, R. Alvarez-Donado, S. Papanikolaou, J. Jagielski, and M. Alava, *Materials & Design* **217**, 110639 (2022).
- <sup>17</sup>K. Frydrych, F. Dominguez-Gutierrez, M. Alava, and S. Papanikolaou, *Mechanics of Materials* **181**, 104644 (2023).
- <sup>18</sup>T. Stasiak, D. Oleszak, and A. Fraczkiewicz, *JOM* **74**, 4842 (2022).
- <sup>19</sup>C. Lu, L. Niu, N. Chen, *et al.*, *Nature Communications* **7**, 13564 (2016).

- <sup>20</sup>K. Jin, C. Lu, L. Wang, J. Qu, W. Weber, Y. Zhang, and H. Bei, *Scripta Materialia* **119**, 65 (2016).
- <sup>21</sup>A. Daramola, G. Bonny, G. Adjanor, C. Domain, G. Monnet, and A. Fraczkiewicz, *Computational Materials Science* **203**, 111165 (2022).
- <sup>22</sup>W. Zhong, S. Hayakawa, H. Xu, K. An, A. Y. Borisevich, J. L. Cicotte, E. P. George, and Y. Yang, *International Journal of Plasticity* **167**, 103663 (2023).
- <sup>23</sup>C. A. Schuh, *Materials Today* **9**, 32 (2006).
- <sup>24</sup>J. Varillas, J. Ocenasek, J. Torner, and J. Alcala, *Acta Materialia* **125**, 431 (2017).
- <sup>25</sup>S. Pathak and S. R. Kalidindi, *Materials Science and Engineering: R: Reports* **91**, 1 (2015).
- <sup>26</sup>L. Yang, Y. Chen, J. Miller, W. J. Weber, H. Bei, and Y. Zhang, *Materials Science and Engineering: A* **856**, 143685 (2022).
- <sup>27</sup>S. Pathak, S. R. Kalidindi, and N. A. Mara, *Scripta Materialia* **113**, 241 (2016).
- <sup>28</sup>T. Remington, C. Ruestes, E. Bringa, B. Remington, C. Lu, B. Kad, and M. Meyers, *Acta Materialia* **78**, 378 (2014).
- <sup>29</sup>E. Wyszowska, C. Mieszczynski, L. Kurpaska, A. Azarov, I. Jalswik, A. Kosinska, W. Chrominski, R. Diduszko, W. Y. Huo, I. Cienlik, and J. Jagielski, *Nanoscale* **15**, 4870 (2023).
- <sup>30</sup>Z. Li, S. Gao, U. Brand, K. Hiller, and H. Wolff, *Nanotechnology* **31**, 305502 (2020).
- <sup>31</sup>F. Dominguez-Gutierrez, *Nuclear Instruments and Methods in Physics Research Section B: Beam Interactions with Materials and Atoms* **512**, 38 (2022).
- <sup>32</sup>S. Hu, T. Fu, Q. Liang, S. Weng, X. Chen, Y. Zhao, and X. Peng, *Frontiers in Materials* **8**, 813382 (2022).
- <sup>33</sup>A. Chandan, S. Tripathy, B. Sen, M. Ghosh, and S. G. Chowdhury, *Scripta Materialia* **199**, 113891 (2021).
- <sup>34</sup>S. Huang, W. Li, S. Lu, F. Tian, J. Shen, E. Holmström, and L. Vitos, *Scripta Materialia* **108**, 44 (2015).
- <sup>35</sup>A. P. Thompson, H. M. Aktulga, R. Berger, D. S. Bolintineanu, W. M. Brown, P. S. Crozier, P. J. in 't Veld, A. Kohlmeyer, S. G. Moore, T. D. Nguyen, R. Shan, M. J. Stevens, J. Tranchida, C. Trott, and S. J. Plimpton, *Computer Physics Communications* **271**, 108171 (2022).
- <sup>36</sup>W. M. Choi, Y. Jo, S. Sohn, *et al.*, *npj Comput Mater* **4**, 1 (2018).
- <sup>37</sup>A. Naghdi, F. J. Dominguez-Gutierrez, W. Y. Huo, K. Karimi, and S. Papanikolaou, "Dynamic nanoindentation and short-range order in equiatomic nicoer medium entropy alloy lead to novel density wave ordering," (2022), arXiv:2211.05436 [cond-mat.mtrl-sci].
- <sup>38</sup>J. Guérolé, W. G. Nöhring, A. Vaid, F. Houllé, Z. Xie, A. Prakash, and E. Bitzek, *Computational Materials Science* **175**, 109584 (2020).
- <sup>39</sup>F. Dominguez-Gutierrez, S. Papanikolaou, A. Esfandiarpour, P. Sobkowicz, and M. Alava, *Materials Science and Engineering: A* **826**, 141912 (2021).
- <sup>40</sup>Q. Xu, A. Zaborowska, K. Mulewska, W. Huo, K. Karimi, F. J. Dominguez-Gutierrez, L. Kurpaska, M. J. Alava, and S. Papanikolaou, *Vacuum* **219**, 112733 (2024).
- <sup>41</sup>J. Silcox and P. Hirsch, *Philosophical Magazine* **4**, 72 (1959).
- <sup>42</sup>M. Landeiro Dos Reis, L. Proville, M.-C. Marinica, and M. Sauzay, *Phys. Rev. Mater.* **4**, 103603 (2020).
- <sup>43</sup>F. J. Domínguez-Gutiérrez, P. Grigorev, A. Naghdi, J. Byggmästar, G. Y. Wei, T. D. Swinburne, S. Papanikolaou, and M. J. Alava, *Phys. Rev. Mater.* **7**, 043603 (2023).
- <sup>44</sup>J. Varillas-Delgado and J. Alcala Cabrelles, *A molecular dynamics study of nanocontact plasticity and dislocation avalanches in FCC and BCC crystals*, PhD dissertation, Universitat Politècnica de Catalunya. Departament de Ciència dels Materials i Enginyeria Metal·lúrgica (2019).
- <sup>45</sup>A. Stukowski, *Modelling and simulation in materials science and engineering* **18** (2010), 10.1088/0965-0393/18/1/015012.
- <sup>46</sup>A. Stukowski, V. V. Bulatov, and A. Arsenlis, *Modelling and Simulation in Materials Science and Engineering* **20**, 085007 (2012).
- <sup>47</sup>N. P. Daphalapurkar and K. Ramesh, *Journal of the Mechanics and Physics of Solids* **60**, 277 (2012).
- <sup>48</sup>S. R. Kalidindi, *Journal of the Mechanics and Physics of Solids* **46**, 267 (1998).
- <sup>49</sup>Y. Shen and D. E. Spearot, *Modelling and Simulation in Materials Science and Engineering* **29**, 085017 (2021).
- <sup>50</sup>I. A. Alhafez, C. J. Ruestes, E. M. Bringa, and H. M. Urbassek, *Journal of Alloys and Compounds* **803**, 618 (2019).
- <sup>51</sup>F. J. Dominguez-Gutierrez, A. Ustrzycka, Q. Q. Xu, R. Alvarez-Donado, S. Papanikolaou, and M. J. Alava, *Modelling and Simulation in Materials Science and Engineering* **30**, 085010 (2022).
- <sup>52</sup>D. Bacon, Y. N. Osetsky, and D. Rodney, *Dislocations in solids* **15**, 1 (2009).